Effects of the radial electric field on the confinement of fast ions in ITER

K. Tani[1], M. Honda[2], T. Oikawa[3] , K. Shinohara[2], Y. Kusama[2] and T. Sugie[2]

1.Nippon Advanced Technology Co.,LTD., Naka, Ibaraki 311-0102 Japan
2.Japan Atomic Energy Agency, Naka Ibaraki 311-0193 Japan,
3.ITER organization, Route de Vinon-sur-Verdon, CS 90 04, 13067 St Paul-Lez-Durance, Cedex, France
E-mail: tani.keiji@jaea.go.jp

Abstract. The effects of a radial electric field (EF) on the losses of alpha particles and NBI fast ions in typical ITER operation scenarios for both error fields due to test blanket modules (TBMs) and toroidal field (TF) ripple were evaluated using an iterative method to execute an orbit-following Monte-Carlo code and a one-dimensional transport code. The EF effect on the loss of fast ions strongly depends on the operation scenario as well as on the error field. The electric field is very significant in the loss of fast ions in a 9MA ITER operation scenario with a higher safety factor and in the error field associated with TBMs. The EF effect in the error field of TF–ripple is very small in any operation scenario. The electric field is much more significant for the loss of NBI fast ions than for that of alpha particles. The radial electric field changes the toroidal precession of fast ions and consequently alter their condition of resonance with the error field, which may account for the EF effect on the loss of fast ions in ITER with TBMs.

PACS numbers: 52.55.Fa, 52.55.Pi, 52.65.Cc, 52-65.Pp

1. Introduction

In connection with the phenomenon of the L/H transition, many researchers have investigated the effects of an electric field, hereafter simply referred to as EF, on neoclassical particle orbits. For example, S.I. Krasheninnikov et al. have investigated the EF effects on ion prompt losses [1]. The EF effects on barely banana-trapped particles have been investigated [2, 3], which indicate that the radial electric field effectively increases the number of banana particles. These studies are basically made in an axi-symmetric magnetic field.

The EF effects on the behaviors of fast ions in a non-axisymmetric magnetic field also have been posited by K. Itoh et al. They investigated the effect of the electric field near the plasma surface on the behavior of fast ions which are locally tapped by the toroidal magnetic field ripple (TF ripple) [4]. They pointed out that the local heat load on the first wall due to the loss of ripple-trapped fast ions can be alleviated by the effect of the electric field on fast-ion trajectory.

Recently, preliminary simulation studies to check the effects of the radial electric field on the confinement of alpha particles in a TBM (Test Blanket Module)

configuration were carried out using a very rough model of an electric potential proportional to an electron temperature of $\Phi = C_\Phi T_e / e$ where C_Φ is an input parameter and e, the electron charge. The results were reported at the 1st Energetic Particle Physics ITPA TG meeting held in Lausanne in 2008. Calculations were performed in a non-inductive steady state H-mode operation with a relatively high safety factor in the central plasma core (a 9MA steady-state ITER scenario [5], hereafter simply referred to as a 9MA-HSF ITER scenario) using an orbit-following Monte-Carlo code developed at the Japan Atomic Energy Agency [6], hereafter simply referred to as the OFMC code. The results show that the confinement of alpha particles is substantially affected by the radial electric field. For example, the power loss is enlarged by a factor of 3 for C_Φ=-1.0. This finding motivates us to investigate further the EF effect upon fast ion confinement using a more realistic electric field in the plasmas.

Basically, the plasma parameters, the plasma rotation and the radial electric field are closely related to each other. Plasma rotation depends on the torque transferred from fast ions to the plasma. Consequently, plasma rotation, the electric field and the slowing down of fast ions should be solved self-consistently to assess reliably the effect of the radial electric field on the confinement of fast ions.

The simulation model for investigating this issue is described in section 2. The calculation conditions are shown in section 3. Some basic effects of the radial electric field on fast-ion trajectory are reviewed in section 4. The calculation results and discussions are described in section 5. The conclusions of the present work are summarized in section 6.

2. Simulation model

In the present work, the confinement of fast ions was investigated using the OFMC code. The profile data of the plasma rotation and the radial electric field were obtained using a one-dimensional, two-fluid (thermal electrons and ions) transport code TASK/TX [7-12] in which the effects of fast ions are taken into account as torque, heat and particle sources.

TASK/TX employs a full set of time-dependent transport equations. The details of the equations that govern radial transport, poloidal rotation and toroidal momentum transport are described in Eqs. (2)-(5) of Ref. [7]. Plasma polarization can emerge in the TASK/TX code owing to the coupling of the two-fluid equations and Maxwell's equations, i.e., the two-fluid equation system. Analyses of plasma polarization as rendered in the code are provided in detail in Ref.[8]. In the present calculations, the polarization and the resulting torque distribution were estimated by the OFMC code as explained in section 3.1 of Ref.[9]. Neoclassical radial particle transport is summarized in Ref.[10]. Neoclassical viscous forces implemented in the poloidal rotation equation, which are estimated by the neoclassical transport module NCLASS, self-consistently give rise to poloidal rotation, the bootstrap current, resistivity, the Ware pinch, neoclassical diffusion and so on, through the coupling with the toroidal rotation equation, the radial force balance equation and the continuity equation. In the present work, the plasma densities are fixed and thus neoclassical particle transport does not appear. The same also holds for turbulent particle transport. The friction forces and their (classical) coefficients are explained in section 2.2 of Ref. [7]. For simplicity of calculation, a single ion species can be treated in the TASK/TX code. We consider a virtual ion species composed of a 50:50 mixture of deuterium (D) and tritium (T). Impurities are neglected, and the momentum pinch was not taken into account in the present TASK/TX calculations.

Here we show only the radial force balance for thermal plasma ions which TASK/TX provides as an approximate, steady-state solution. If the electric potential is constant on a magnetic surface, the plasma pressure, the plasma rotation and the radial electric field satisfy the following radial force balance;

$$F_{pot} + F_{prs} + F_{pol} + F_{tor} = 0 . \qquad (1)$$

In a circular cross-sectional plasma, the above forces are described as follows;

$$F_{pot} = -q_i n_i \frac{\partial \Phi(\rho)}{a \partial \rho}, \qquad (2\text{-}1)$$

$$F_{prs} = -\frac{\partial n_i T_i}{a \partial \rho}, \tag{2-2}$$

$$F_{pol} = q_i n_i v_\theta(\rho) B_\phi, \tag{2-3}$$

$$F_{tor} = -q_i n_i v_\phi(\rho) B_\vartheta, \tag{2-4}$$

where ρ is the radius normalized by the minor radius a; v_ϕ and v_θ are the toroidal and poloidal rotation velocities, respectively; Φ is the electric potential; q_i is the charge of plasma ions; and B_θ and B_ϕ are the poloidal and toroidal magnetic fields, respectively.

Because TASK/TX is a time-dependent transport code, we approximate the above force balance near the flat top in a time-dependent solution. In order to maintain the distribution of plasma density and temperature, we chose the option in TASK/TX of solving transport equations with fixed density and temperature profiles.

For the above calculation, TASK/TX needs the input data of the torque distribution which is calculated by the OFMC code. For the calculation of the torque transferred from fast ions to bulk plasma during the slowing down of fast ions, OFMC needs the profile data for the electric potential and the toroidal and poloidal rotation velocities which are the output of TASK/TX. Therefore, we executed the OFMC and TASK/TX codes in an iterative and alternating manner.

For the calculation of the plasma rotation using the torque data from the OFMC code, the toroidal momentum diffusivity χ_ϕ is given in the TASK/TX code as,

$$\chi_\phi = \mathrm{Pr}\, \chi_{i-CDBM} \tag{3}$$

where χ_{i-CDBM} is the heat diffusivity based on the Current Diffusive Ballooning Mode (CDBM) and the Prandtl number Pr is an input parameter [11]. More information about the toroidal momentum diffusivity used in TASK/TX can be found in the references [7,12,13].

The process for calculating the Coulomb collisions of fast ions in a rotating plasma is as follows. If the plasma is rotating along the magnetic field line at velocity $v_{//rot}$, the velocity components of fast ions parallel and vertical to the magnetic field line in the rotating frame $v_{//}^*$ and $v_\perp^*$ can be expressed with the velocity components in the rest

frame $v_{//}$ and $v_{\perp}$, as

$$v_{//}^{*} = v_{//} - v_{//rot}, \tag{4-1}$$

$$v_{\perp}^{*} = v_{\perp}. \tag{4-2}$$

The plasma rotation velocity $v_{//rot}$ is given by

$$v_{//rot} = \frac{B_{\phi}}{B} v_{\phi} + \frac{B_{p}}{B} v_{p}, \tag{4-3}$$

where B_p and v_p are the poloidal magnetic field and the poloidal rotation velocity in a non-circular plasma; and $B = \sqrt{B_{\phi}^2 + B_p^2}$. If we assume that the distribution of bulk plasma particles is Maxwellian in the rotating frame, then the collision operators given by Trubnikov [6, 14] are applicable. As such, in the rotating frame, the new velocity components of a test particle following Coulomb collisions with bulk plasma particles can be given by

$$v_{//col}^{*} = v_{//}^{*} + \Delta v_L \frac{v_{//}^{*}}{v^{*}} + \Delta v_T \frac{v_{\perp}^{*}}{v^{*}} \sin\Omega, \tag{4-4}$$

$$v_{\perp col}^{*} = \sqrt{(v^{*} + \Delta v_L)^2 + \Delta v_T^2 - v_{//col}^{*2}}, \tag{4-5}$$

where $v^{*} = \sqrt{v_{//}^{*2} + v_{\perp}^{*2}}$ is the total velocity of the test particle before a collision; Ω, the Larmor phase; Δv_L, the longitudinal component of the velocity change; and Δv_T, the transverse component [14]. Using the above equations, the new velocity components for the test particle in the rest frame can be given as

$$v_{//new} = v_{//col}^{*} + v_{//rot}, \tag{4-6}$$

$$v_{\perp new} = v_{\perp col}^{*}. \tag{4-7}$$

The above calculations were executed at every $10^{-7}\tau_s$, where τ_s is the slowing down time at the plasma center.

Note that the effects of the plasma rotation on Coulomb collisions for energetic particles are generally very small.

3. Calculation conditions

3.1 Calculation parameters

Calculations were made for the plasma parameters appropriate to the 9MA ITER scenario with a higher safety factor in the central plasma core (9MA-HSF) [5] in which the loss of energetic particles due to the error field of TBMs is significant. For comparison, calculations also were made for the plasma parameters appropriate to the 9MA ITER scenario with a lower safety factor in the central plasma core (9MA-LSF) and 15MA scenario [15].

The major plasma parameters for the above three operation scenarios are summarized in table 1. The radial distribution of the plasma density, the ion and electron temperatures for 9MA-HSF, 9MA-LSF and 15MA are shown in figure 1(A-1), (A-2) and (A-3), respectively. The D and T temperature profiles are equivalent to T_i in each operation scenario. The ion density profiles were calculated assuming a 50-50 mixture of D and T and the charge neutrality condition. In figure 1, the radial position is described by the poloidal flux function normalized by the value at the plasma surface ψ / ψ_a. The radial distribution of the safety factor and the MHD equilibrium for 9MA-HSF, 9MA-LSF and 15MA are also shown in figure 1 (B-1,2 and 3) and (C-1,2 and 3), respectively.

Table 1 Plasma parameters for typical ITER operation scenarios

		9MA-HSF (High Safety Factor)	9MA-LSF (Low Safety Factor)	15MA
Major radius of plasma axis	R_t	6.69m	6.67m	6.42m
Minor radius	a	1.84m	2.0m	2.0m
Toroidal field @R=Rt	B_t	4.91T	4.93T	5.12T
Plasma parameters at plasma center				
Electron density	n_{e0}	7.27×10^{19} m^{-3}	7.22×10^{19} m^{-3}	1.13×10^{20} m^{-3}
Electron temperature	T_{e0}	23.9 KeV	34.3 KeV	27.0 KeV
Ion densities	$n_{D0}=n_{T0}$	2.19×10^{19} m^{-3}	2.82×10^{19} m^{-3}	4.44×10^{19} m^{-3}
Ion temperatures	$T_{D0}=T_{T0}$	25.2 KeV	31.3 KeV	23.5 KeV
Total Plasma current	I_p	9MA	9MA	15MA
Safety factors				
at plasma center	$q_{s\text{-}ax}$	3.26	1.84	1.03
near plasma edge @ψ/ψ_a=0.95	$q_{s\text{-}95}$	5.11	5.88	3.22
Ellipticity	κ	1.96	1.84	1.85
Triangularity	δ	0.55	0.47	0.47
Effective Z (uniform)	Zeff	2.19	1.65	1.64
Impurity species		Beryllium	Beryllium	Beryllium

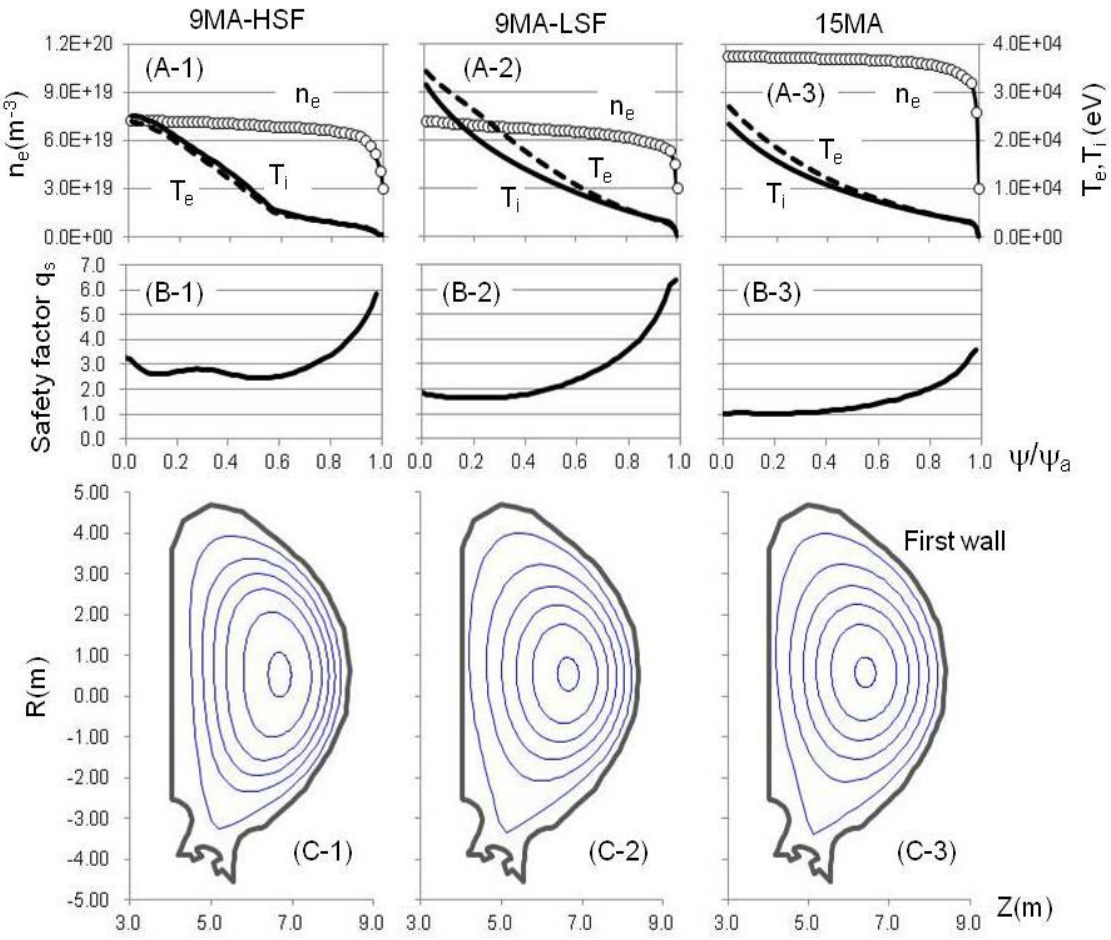

Figure 1 Distribution of the plasma density, the ion and electron temperatures and the MHD equilibrium for the ITER 9MA scenario with a higher safety factor (9MA-HSF) are shown in (A-1) and (B-1) and (C-1), respectively. Those for the 9MA scenario with a lower safety factor (9MA-LSF) are shown in (A-2) and (B-2) and (C-2) and those for 15MA scenario in (A-3) and (B-3) and (C-3), respectively.

3.2 Non-axisymmetric magnetic field

We used the fully 3-D vacuum magnetic fields caused by the finite number of TF coils, ferromagnetic components and/or TBMs as provided by the ITER Organization [16]. The magnetic fields were tabulated and used in the OFMC code with a 3-D cubic spline interpolation method. The interpolated vacuum ripple field is superposed to the axisymmetric field calculated with the 2D MHD equilibrium shown in figure 1 (C-1), (C-2) and (C-3).

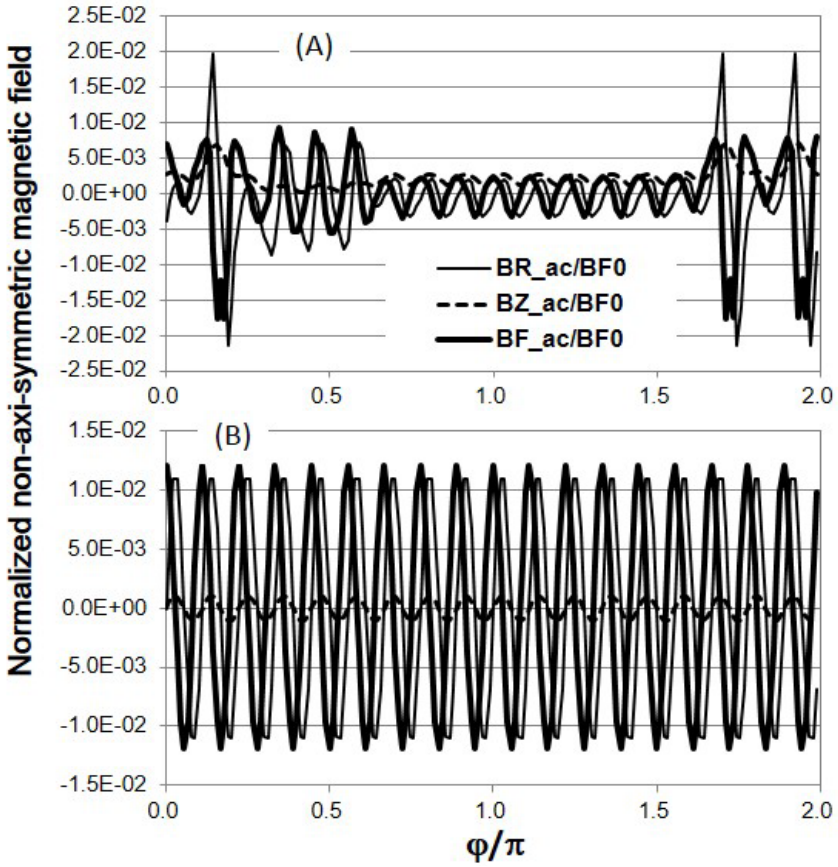

Figure 2 Distribution of the non-axisymmetric components of vacuum magnetic fields normalized by the toroidal magnetic field on axis along the toroidal angle at the outer edge of the plasma for TBMs (A) and TF-ripple (B).

Calculations were made for the following two different cases of non-axisymmetric magnetic fields.

Case TBM; error field due to three TBMs and 18 TF coils with ferromagnetic inserts (FIs), and

Case TFR; error field only from 18 TF coils without FIs.

For reference, the non-axisymmetric components of vacuum magnetic fields normalized by the troroidal magnetic field on axis along the toroidal angle at the outer edge of the plasma for the Case TBM are shown in figure 2(A) and those for the Case TFR in figure 2(B). There are three large ripples in (A) which correspond to those due to TBMs. There are three medium size ripples at the vacuum-vessel sectors for the NBI ports where FIs are not installed. The other small ripples are those at the vacuum-vessel sectors with FIs.

Figure 3 shows the distribution of the field ripple defined by $(B_{\max} - B_{\min})/(B_{\max} + B_{\min})$ on the plasma surface along the poloidal angle for both error

fields due to TBMs and TF ripple where B_{max} and B_{min} are the maximum and minimum magnetic fields along the toroidal angle.

Note that the non-axisymmetric values for the magnetic field used in the present work are somewhat larger than the most recent data from ITER. However, the discrepancy in these values does not essentially change the basic behavior of fast ions.

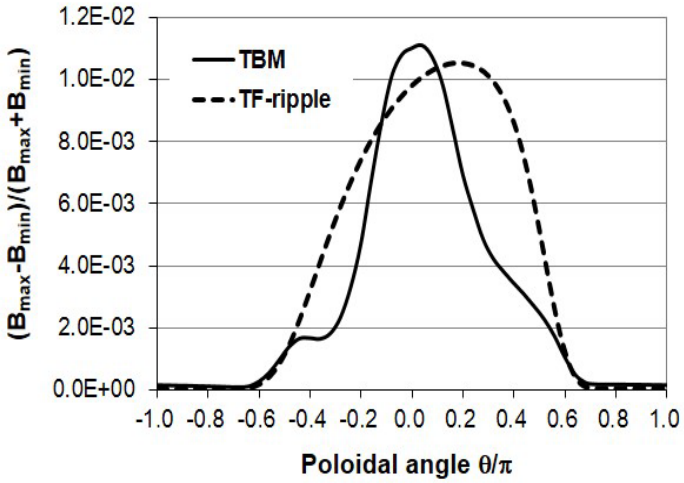

Figure 3. Distribution of field ripple on the plasma surface along the poloidal angle for the error fields due to TBMs and TF ripple.

3.3 Fast ions

The effects of the electric field on the confinement of fast ions produced by fusion reactions as well as those produced by neutral beam injection (NBI) were investigated.

Monte Carlo techniques were applied to generate test alpha particles with a birth energy of 3.5MeV [17, 21]. For each test particle, the initial birth flux surface was fixed with a uniform random number taking the radial distribution of the fusion reaction rate and the plasma volume into account. For the radial position, the poloidal angle was also fixed with another random number, taking the poloidal magnetic field and the poloidal differential path length along the birth flux surface into account.

Monte Carlo techniques were also applied to generate the test particles of NBI fast ions assuming two finite-volume beam lines with injection angles and beam energies equivalent to those of the two multi-beamlet NB injectors of ITER [18]. ITER employs two tangential injection systems with 1.0MeV D beams (0.87MeV H beams).

For reference, the birth profiles of alpha particles are shown in figure 4(A) as functions of the normalized minor radius ρ for the operation scenarios 9MA-HSF, 9MA-LSF and 15MA by the solid, dashed and dotted curves, respectively. The birth

profiles of NBI fast ions are shown also in figure 4(B).

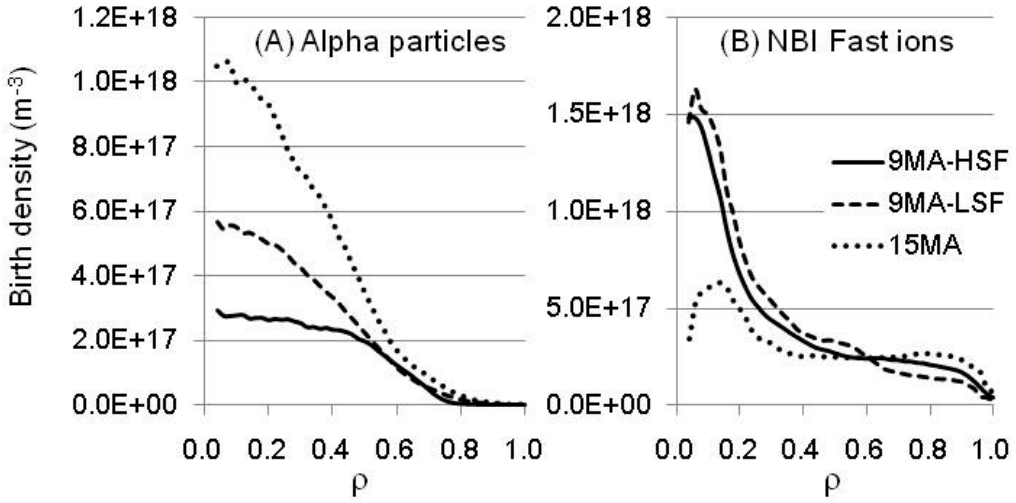

Figure 4. Birth profiles of alpha particles (A) and NBI fast ions (B) as functions of the normalized minor radius. Birth profiles in the operation scenarios 9MA-HSF, 9MA-LSF and 15MA are shown by the solid, dashed and dotted curves, respectively.

3.4 First wall geometry

ITER employs a very complicated 3D first wall with two limiter-like convex areas in each toroidal sector [19]. The first wall geometry was exactly reproduced in the OFMC code.

4. Review of the basic effects of the radial electric field on fast-ion trajectory

Generally, fast ions are well confined in axi-symmetric tokamaks and are lost to the first wall mainly due to the non-axisymmetric component of the magnetic field [20, 21]. It is well-known that the non-axisymmetric magnetic field mainly affects the trajectories of banana-trapped fast ions in particular at their banana-tip points [22,23]. Here we summarize the EF effects on the neoclassical fast ion trajectory with a particular focus on the banana-tip point, a focus which may be helpful in qualitatively understanding the results from the OFMC-TASK/TX simulation in section 5.

4.1 Effect of the radial electric field on banana-tip position [24]

If we consider a fast ion with initial velocities parallel and perpendicular to the magnetic field line $(v_{//0}, v_{\perp 0})$ on the mid-plane at $R = R_0$ where $\psi = \psi_0$, then the energy conservation condition gives

$$\frac{1}{2} m_f v_0^2 + e_f \Phi(\psi_0) = \frac{1}{2} m_f (v_{//}^2 + v_{\perp}^2) + e_f \Phi(\psi) \qquad (5)$$

where variables without the suffix 0 indicate those on the trajectory, $v_0 = \sqrt{v_{//0}^2 + v_{\perp 0}^2}$, m_f and e_f are the mass and the charge of the fast ion, respectively.

Conservation of the canonical angular momentum gives

$$P_\phi = e_f (\psi_0 + \Delta\psi) \quad \text{(const.)} \qquad (6)$$

where

$$\Delta\psi = -\frac{m_f}{e_f} R_0 v_{//0}. \qquad (7)$$

Conservation of the magnetic moment gives

$$\frac{m_f v_{\perp 0}^2}{2B(R_0)} = \frac{m_f v_{\perp}^2}{2B(R)}$$

If the banana size is small enough,

$$\Phi(P_\phi) \cong \Phi(\psi_0) + \frac{\partial \Phi}{\partial \psi} \Delta\psi \,. \qquad (8)$$

If the poloidal magnetic field is much smaller than the toroidal field, conservation of the magnetic moment at the banana tip gives

$$\frac{m_f}{2} v_{\perp}^2 = \frac{m_f}{2} v_{\perp 0}^2 \frac{R_0}{R_{tip}} \tag{9}$$

From equations (5), (8) and (9),

$$W_0 = \frac{1}{2} m_f v_0^2 = \frac{m_f}{2} v_{\perp 0}^2 \frac{R_0}{R_{tip}} + e_f \frac{\partial \Phi}{\partial \psi} \Delta \psi$$

$$R_{tip} = \frac{\frac{m_f}{2} v_{\perp 0}^2 R_0}{\frac{m_f}{2} v_0^2 - e_f \frac{\partial \Phi}{\partial \psi} \Delta \psi} \tag{10}$$

Equation (6-10) gives

$$R_{tip} \cong R_{tip}^* + \Delta R_{tip}^{EF}$$

where $R_{tip}^* (= R_0 v_{\perp}^2 / v_0^2)$ is the banana tip point without the electric field, and

$$\Delta R_{tip}^{EF} \cong R_{tip}^* \frac{e_f \frac{\partial \Phi}{\partial \psi} \Delta \psi}{W_0} \tag{11}$$

The trajectories of counter banana particles near the tips are shown in figure 5(A) for the radial electric fields $E_r \approx +10 kV/m$, $E_r = 0.0$ and $E_r \approx -10 kV/m$, using thin, dotted and thick curves, respectively. Note that the radial shift of the banana tip due to the electric field depends on the initial parallel velocity. If the electric field is negative and the particle is counter ($v_{//0} / v_0 = -0.174$), the banana tip moves outward, i.e., into a higher error field region

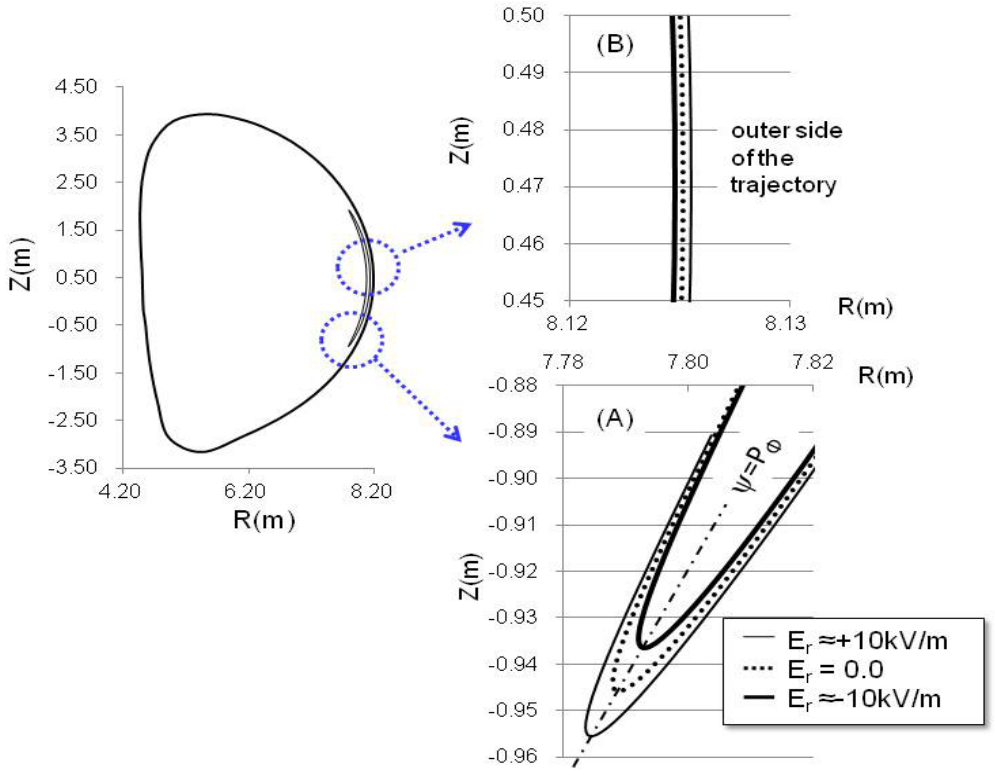

Figure 5. The trajectories of counter banana particles near the tips for three radial electric fields: $E_r \approx +10kV/m$, $E_r = 0.0$ and $E_r = -10kV/m$ are shown using thin, dotted and thick curves in (A), respectively. Corresponding trajectories near the outer edge are shown in (B).

4.2 Effect of the electric field on the banana width

If we assume that a banana particle starts from the midplane at $R = R_0$ with velocities parallel and perpendicular to the magnetic field line $(v_{//0}, v_{\perp 0})$ and returns to the midplane at $R = R_0 + \rho_B$ with velocities $(v'_{//0}, v'_{\perp 0})$ after a half bounce motion, the canonical angular momentum conservation condition gives

$$v'_{//0} \approx v_{//0} + \left(\frac{e_f}{m_f} B_{p0} - \frac{v_{//0}}{R_0} \right) \rho_B , \tag{12}$$

where B_{p0} is the poloidal magnetic field on the midplane. The magnetic-moment conservation gives

$$v'^2_{\perp} \approx v^2_{\perp 0} \left[1 - \frac{\rho_B}{R_0} + \left(\frac{\rho_B}{R_0} \right)^2 \right] . \tag{13}$$

The energy conservation gives

$$v_{//0}^2 + v_{\perp 0}^2 \approx v_{//0}'^2 + v_{\perp 0}'^2 + \frac{2e_f}{m_f}\frac{\partial \Phi}{\partial R}. \tag{14}$$

Substituting the parallel and perpendicular velocities given by equations (12) and (13) into equation (14), we obtain a non-zero ρ_B solution as

$$\rho_B = \frac{-2v_{//0}\left(\frac{e_f}{m_f}B_{p0} - \frac{v_{//0}}{R_0}\right) - \frac{v_{\perp 0}^2}{R_0} - \frac{2e_f}{m_f}\frac{\partial \Phi}{\partial R}}{\left(\frac{e_f}{m_f}B_{p0} - \frac{v_{//0}}{R_0}\right)^2 + \left(\frac{v_{\perp 0}}{R_0}\right)^2} \tag{15}$$

If we apply an ordering for banana-trapped alpha particles in ITER, the particle velocity $v_0 = 1.3\times 10^7 m/s$, the velocity pitch $v_{//0}/v_0 = -0.3$, $B_{p0} \approx 0.3T$ and $R_0 \approx 6.0m$, then

$$\left|\frac{e_f}{m_f}B_{p0}\right| >> \left|\frac{v_{//0}}{R_0}\right|, \quad \left|\frac{e_f}{m_f}B_{p0}\right| >> \left|\frac{v_{\perp 0}}{R_0}\right| \quad \text{and} \quad \left|2v_{//0}\frac{e_f}{m_f}B_{p0}\right| > \left|\frac{v_{\perp 0}^2}{R_0}\right|.$$

The above ordering gives

$$\rho_B \approx \rho_B^* + \Delta\rho_B^{EF}$$

where

$$\rho_B^* = -\frac{2m_f}{e_f}\frac{v_{//0}}{B_{p0}} \tag{16}$$

$$\Delta\rho_B^{EF} = -\frac{2m_f}{e_f}\frac{1}{B_{p0}^2}\frac{\partial \Phi}{\partial R} \tag{17}$$

Note that the banana width given by equation (16) agrees with the well-known equation. Also note that the change in the banana width due to the electric field depends only on the electric field and the poloidal magnetic field which are independent of the particle velocity. Trajectories of banana particles near the outer midplane are shown in figure 5 (B) for the radial electric fields, $E_r \approx +10kV/m$, $E_r = 0.0$ and $E_r = -10kV/m$, using thin, dotted and thick curves, respectively. If the electric field is negative the banana width shrinks, i.e., the direct loss region becomes smaller.

4.3 Effect of the radial electric field on fast-ion toroidal precession [24, 25, 26]

In a tokamak system, fast ions move along toroidally precessional trajectories caused by the ∇B drift. In the presence of an electric field, the $E \times B$ drift also causes toroidal precession. The toroidal angle change after one bounce of motion of a banana particle is given by

$$\varphi_{tpc} = \varphi_{tpc}^{\nabla B} + \varphi_{tpc}^{EF} \tag{18}$$

where $\varphi_{tpc}^{\nabla B}$ and φ_{tpc}^{EF} are the toroidal precession caused by the ∇B drift and the $E \times B$ drift, respectively.

In a circular plasma, they are approximately given by

$$\varphi_{tpc-Circ}^{\nabla B} \approx 2\sqrt{2}\frac{U}{v}\frac{q_s^2}{r\sqrt{\varepsilon}}\left[2E(\xi) - K(\xi)\right] \tag{19}$$

$$\varphi_{tpc-Circ}^{EF} \approx 4\sqrt{2}\frac{q_s^2 E_r}{v\varepsilon^{3/2}}K(\xi) \tag{20}$$

where

$$U = \frac{m_f}{e_f}\left(\frac{2v_{//}^2 + v_{\perp}^2}{2B}\right),$$

$K(\xi)$ and $E(\xi)$ are the first and the second kind of complete elliptic integrals,

$$\xi = \sin\frac{\theta_b}{2},$$

θ_b is the poloidal angle of the banana-tip point, q_s is the safety factor and ε is the inverse aspect ratio.

If $\left|\varphi_{tpc}^{EF}\right|$ is much smaller than $\left|\varphi_{tpc}^{\nabla B}\right|$, the difference between minor radii with equal toroidal precession angles in systems with and without the EF can be given as

$$\varphi_{tpc}^{\nabla B}(r - \Delta r_{tpc}^{EF}) \approx \varphi_{tpc}^{\nabla B}(r) + \varphi_{tpc}^{EF}(r)$$

$$\Delta r_{tpc}^{EF} \approx -\varphi_{tpc}^{EF}\Big/\frac{\partial \varphi_{tpc}^{\nabla B}}{\partial r} \tag{21}$$

5. Calculation results and discussion

5.1 Results from the OFMC-TASK/TX iterative method

Calculations start with the OFMC code without the electric field and plasma rotation. The OFMC code produces among its outputs the distribution of torque transferred from fast ions to bulk plasma. Using the torque distribution data, TASK/TX produces the time-dependent radial distribution of the electric potential and rotation velocities. The radial electric field and the rotation velocities depend on the toroidal momentum diffusivity χ_ϕ. The impact of the Prandtl number on the confinement of NBI-produced fast ions in which the plasma rotation plays an important role was checked for the operation scenario 9MA-HSF. The radial distribution of the toroidal rotation velocity after one OFMC-TASK/TX iterative calculation step for Pr=1.0, 1.4 and 1.8 is shown in figure 6(A) by the dotted, solid and dashed curves, respectively. The distribution of the electric potential is also shown in figure 6(B). For the calculation conditions described in section 3, we found that the distribution of the electric potential and the rotation velocities with Pr=1.0, 1.4 and 1.8 were saturated at about t=2.0s, 3.0s and 4.0s, respectively.

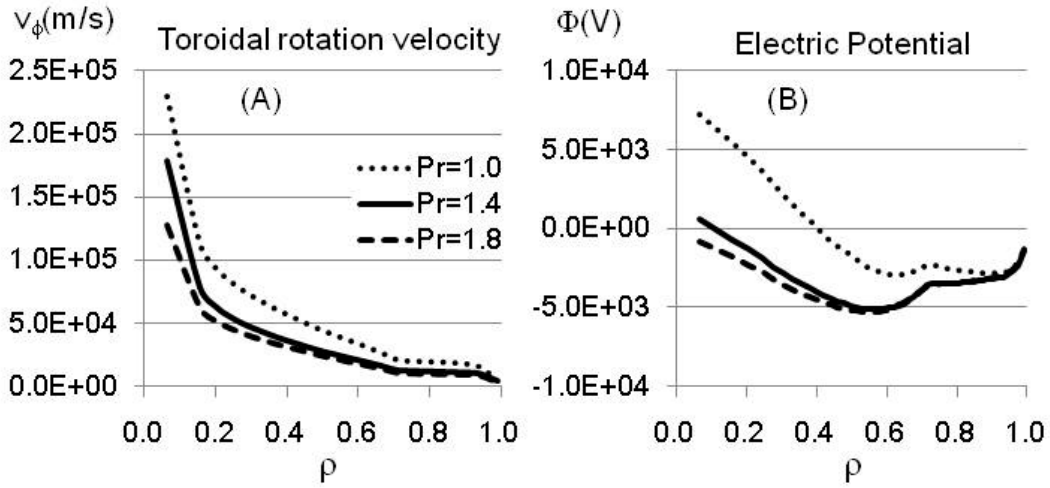

Figure 6 Radial distribution of the toroidal rotation velocity (A) and the electric potential (B) after one OFMC-TASK/TX iterative calculation step for NBI fast ions in the operation scenario 9MA-HSF. The results for Pr=1.0, 1.4 and 1.8 are shown by the dotted, solid and dashed curves, respectively.

The dependence of the power loss on the Prandtl number is shown in figure 7. Figure 6(B) reveals that the global distribution of the electric potential substantially depends on the Pr number. The loss of fast ions, however, shows rather weak dependence on the Pr number and saturates with it. Note that the distribution of the electric potential for Pr=1.4 is similar to that for Pr=1.8 particularly near the plasma periphery. Judging from

the results shown in figure 7 and the distribution of the electric potential shown in figure 6(B), the radial electric field near the plasma edge plays a significant role in the loss of fast ions. Taking the above results into consideration, we assume $P_r = 1.4$ as a standard value for the following numerical studies. This Prandtl number is consistent with the recent database on momentum transport which indicates that P_r can be greater than unity in a low collisionality region [27].

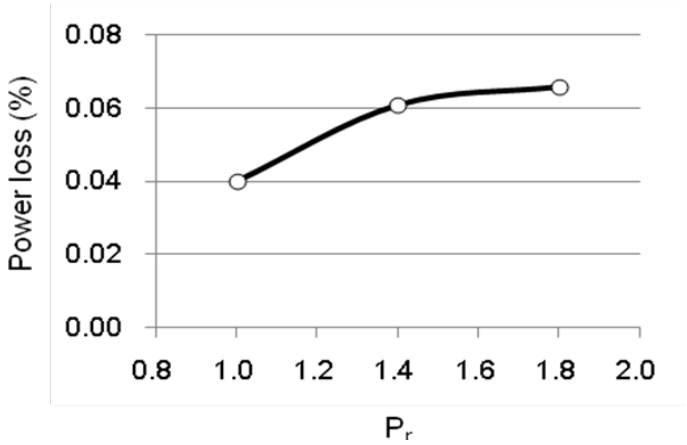

Figure 7 Dependence of the loss of NBI-produced fast ions on the Prandtl number.

Simulation studies were made for several combinations of the three operation scenarios and the two different kinds of error fields described in section 3. The results are described separately in subsection 5.1.1 for the error field from TBMs (Case TBM) and those for the toroidal field ripple (Case TFR) in subsection 5.1.2.

5.1.1 Case TBM

In most operation scenarios of ITER employing D and T mixed bulk plasma ions and NBI injection for heating and current drive, energetic alpha particles and NBI-produced fast ions coexist and jointly generate torque in the plasma. As the first step of the TASK/TX-OFMC calculation, the torque sources from alpha particles and NBI fast ions are separately taken into consideration, and the results are described in the next subsection (1). The results for the joint torque produced by the NBI-Alpha combined heating are shown in subsection (2).

(1) Separate alpha-particle and NBI heating

The radial distribution of the torque densities driven by separate alpha-particle and NBI heating as calculated by the OFMC code at the first iteration step are shown in figure 8 for each operation scenario; (A) for 9MA-HSF, (B) 9MA-LSF and (C) 15MA. The solid lines show the torque densities driven by the NBI fast ions only and the dotted

line, by alpha particles only. Note that the torque density distribution shown in figure 8 remains nearly unchanged in subsequent iteration steps due to the reason described below.

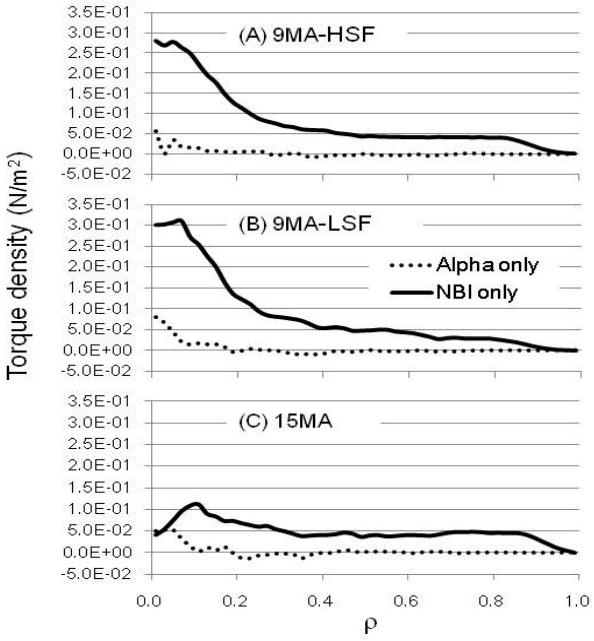

Figure 8 The radial distribution of the torque densities driven by separate alpha-particle and NBI heating as calculated by the OFMC code at the first iteration step for each operation scenario; (A) for 9MA-HSF, (B) 9MA-LSF and (C) 15MA.

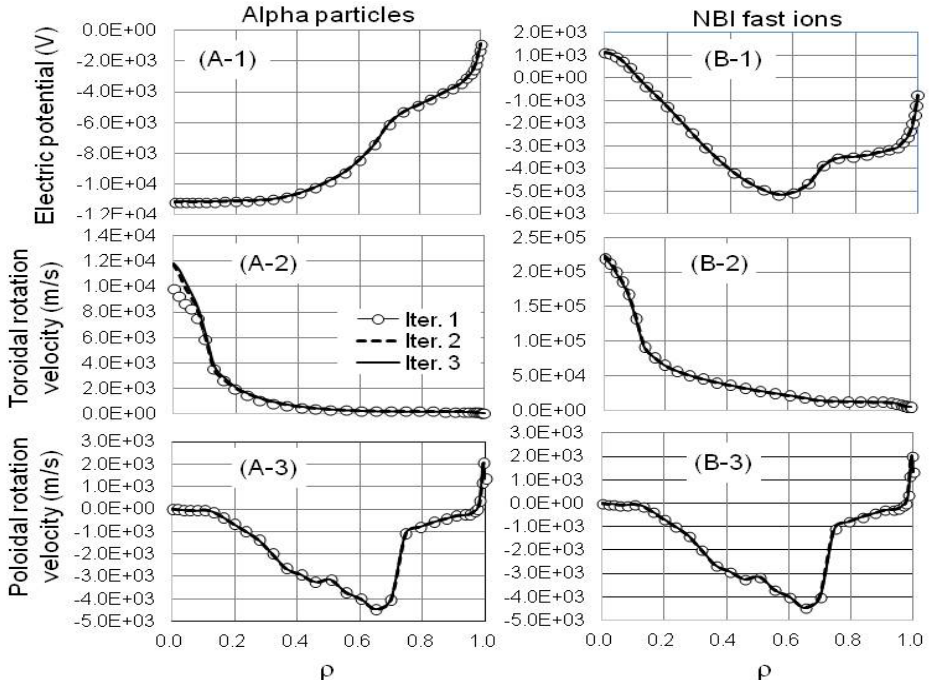

Figure 9. Radial distribution of the electric potential, the toroidal and poloidal rotation velocities in the operation scenario 9MA-HSF at every iterative step for alpha particles in (A-1), (A-2) and (A-3) and. for NBI fast ions in (B-2), (B-2) and (B-3), respectively.

The radial distribution of the electric potential and the toroidal and poloidal rotation velocities in the operation scenario 9MA-HSF which are driven by the torque from alpha particles only at every step in the iteration are shown in figure 9(A-1), (A-2) and (A-3) and those driven by torque from NBI fast ions in figure 9(B-1), (B-2) and (B-3), respectively.

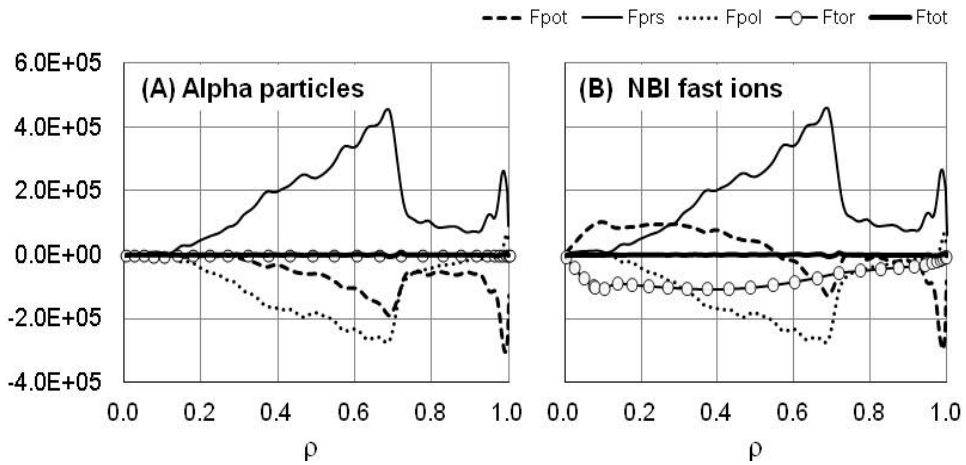

Figure 10. Force balance at the third iteration step for alpha particles (A) and NBI fast ions (B).

The force balance described by equation (1) for alpha particles at the third step in the iteration is shown in figure 10(A) and that for NBI fast ions in (B). The dashed line, the thin solid line, the dotted curves and the open circles in figure 10 show the distributions of the following variables, respectively: the force of electric field F_{pot}, the pressure gradient F_{prs}, the poloidal rotation F_{pol} and the toroidal rotation F_{tor}. The total sum of these forces F_{tot} is also shown by the thick solid line. As shown in figure 10, F_{tot} is approximately zero for both alpha particles and NBI fast ions, which indicates that these forces are well balanced. Figure 10 also shows that the poloidal rotation velocity is approximately given by the plasma parameters and is independent of the iterative steps for both alpha particles and NBI fast ions. Since the birth velocity-distribution of alpha particles is isotropic, the alpha-driven torque and the resulting toroidal rotation velocity are much smaller than those of fast ions produced by a directional NBI [9,13]. Consequently, the distribution of the electric field for alpha particles is approximately given by the force of the pressure gradient F_{prs} and that of

the poloidal rotation F_{pol}. On the other hand, the force of toroidal rotation F_{tor} shows a substantial effect on the electric field for NBI fast ions near the plasma center where the rotation velocity is very large as shown in figure 9(B-2).

Note that the radial distribution of the rotation velocities and the electric potential reach convergent states after only one iterative step. This finding implies that the effects of both the radial electric field and the plasma rotations are not large enough to be affected via fast-ion transport.

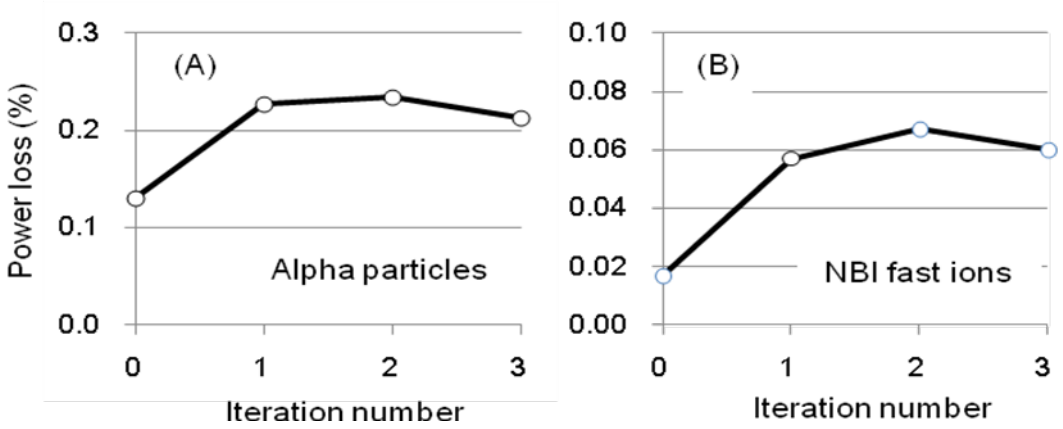

Figure 11. Change of power loss at every iterative step in the operation scenario 9MA-HSF for alpha particles (A) and NBI fast ions (B).

Changes in the power loss of alpha particles and of NBI fast ions with the iterative steps corresponding to those in figure 9 are shown in figure 11(A) and (B), respectively. Both power loss fractions reach convergence after only one iterative step. In the case of TBM, the electric field is very significant in the loss of fast ions, though the power loss fractions are small.

The effects of the radial electric field for the other operation scenarios were also estimated through the same calculation method described above. Figure 12(A) and (B) show the steady-state radial electric field along the major radius on the midplane from the plasma center to the edge in each operation scenario for alpha particles and NBI fast ions, respectively. In most cases, large negative peaks are observed near the plasma edge. Only in the case of 9MA-HSF does another peak appear near $R \approx 7.8m$, which may be significant for the loss of fast ions because their birth profiles are center-peaked as shown in figure 4. As described in section 1, we have previously estimated the effect of the radial EF on the loss of alpha particles in the operation scenario 9MA-HSF using a rough model of an electric potential $\Phi(\psi) = -T_e(\psi)/e$. We found that the distribution of the electric field obtained by TASK/TX for the same operation scenario which is

shown by the solid curve in figure 12(A) is much smaller than the electric field used in the previous work by a factor of 0.2-0.5, depending on the radial position. This indicates that the previous results over-estimated the effect of the radial EF on the loss of alpha particles.

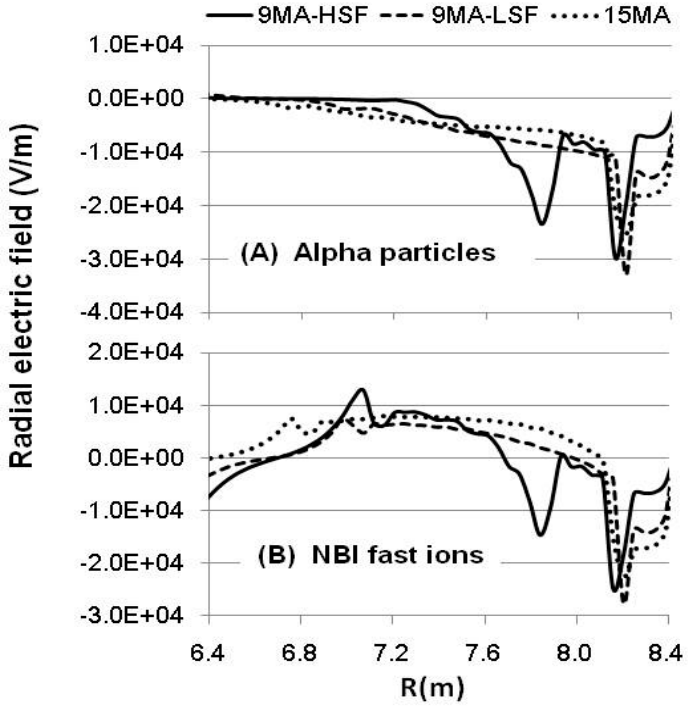

Figure 12. Steady-state distribution of the radial electric field along the major radius on the midplane from the plasma center to the edge in the operation scenarios 9MA-HSF, 9MA-LSF and 15MA for alpha particles (A) and for NBI fast ions (B).

The results regarding the loss of fast ions with and without the effects of the EF are summarized in table 2 for all operation scenarios for separate NBI and alpha-particle heating. Here we define an enlargement factor as a ratio of the power loss fraction with the electric field to that without the field. The enlargement factor is also shown in the 6^{th} column in table 2. For reference, the losses of alpha particles in an axisymmetric field for 9MA-HSF are also shown in table 2. As described in the beginning of section 4, alpha particles are well confined in an axi-symmetric field. The effect of the radial electric field on the loss seems to be very small. As shown in table 2, the EF enlargement factor strongly depends on both the operation scenario and the fast ion species. The electric field is very significant in the loss of alpha particles in the case of 9MA-HSF/TBM in which the EF enlargement factor is about 1.7, whereas it is less important for both the 9MA-LSF/TBM and 15MA scenarios. Judging from the results for the cases of 9MA-HSF/TBM and 15MA, the electric field also seems to be very

significant in the loss of NBI fast ions. This may come from the beam deposition near the plasma edge shown in figure 4(B). It should be noted that the losses in the two cases are basically very small. Even if the losses are enlarged by the effects of the electric field, they are still acceptably small.

Table 2 Summary of power losses of fast ions in non-axisymmetric magnetic fields for typical ITER operation scenarios with and without the electric field produced by separate NBI and alpha-particle heating.

Operation scenario	Magnetic field	Fast ions	Power loss w/o EF (%)	Power loss w/ EF (%)	EF-Enlargement factor
9MA-HSF (Higer safety factor)	Axi-symmetric	Alpha	0.029	0.031	1.07
	TBM	Alpha	0.13	0.23	1.73
		NBI	0.017	0.061	3.61
	TFR (TF-Ripple)	Alpha	5.60	6.03	1.08
		NBI	2.30	2.56	1.11
9MA-LSF (Lower safety factor)	TBM	Alpha	0.48	0.50	1.04
		NBI	0.015	0.083	5.53
	TFR	Alpha	3.31	3.60	1.09
15MA	TBM	Alpha	0.072	0.066	0.92
		NBI	0.0034	0.021	6.18

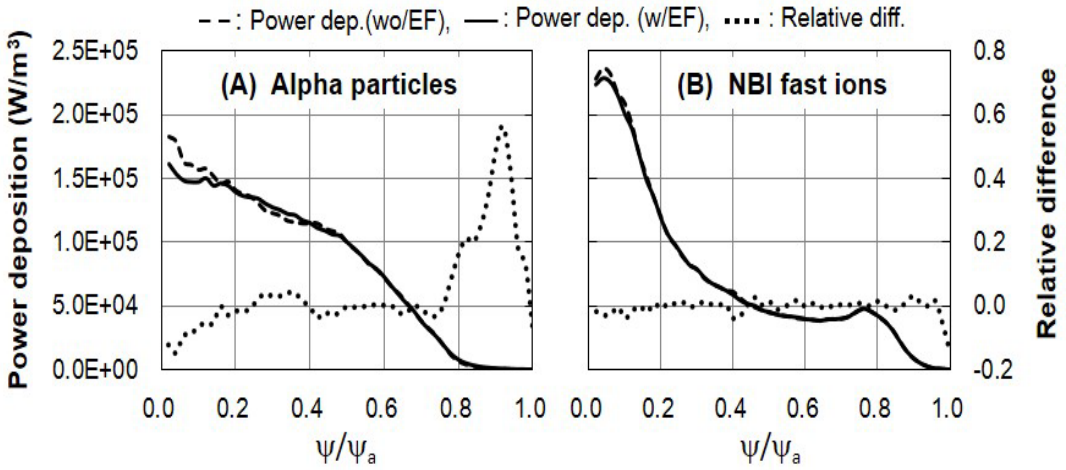

Figure 13 Distribution of the power deposited to bulk plasma in the operation scenario 9MA-HSF with and without the electric field for alpha particles (A) and for NBI fast ions (B).

Concerning the radial electric field, the effect not only on the power loss described above but also on the power deposition profile of fast ions during slowing down is important. The distribution of the alpha power deposited to bulk plasma in the operation scenario 9MA-HSF with and without the electric field is shown in figure 13 (A) by the solid and dashed curves, respectively. The difference between the deposited

power with and without the electric field as normalized by the latter is also shown in figure 13(A) by the dotted curve. Figure 13(A) shows the substantial effect of the electric field on the power deposition of alpha particles not only near the plasma edge but also near the plasma center. The results for NBI power corresponding to the alpha particles described above are also shown in figure 13(B). In the case of NBI power, the effect of the electric field is localized very close to the plasma edge.

(2) NBI and alpha-particle combined heating

In the NBI and alpha-particle combined heating, the torque distribution obtained due to the effect of NBI and alpha-particle heating considered separately as shown in figure 8 were combined. The losses of alpha particle and NBI fast ions were calculated separately by the OFMC code using the same electric field calculated by TASK/TX with the unified torque.

Here we calculated combined heating only for the steady-state operation scenarios of 9MA-HSF and 9MA-LSF in which the losses of fast ions are significant.

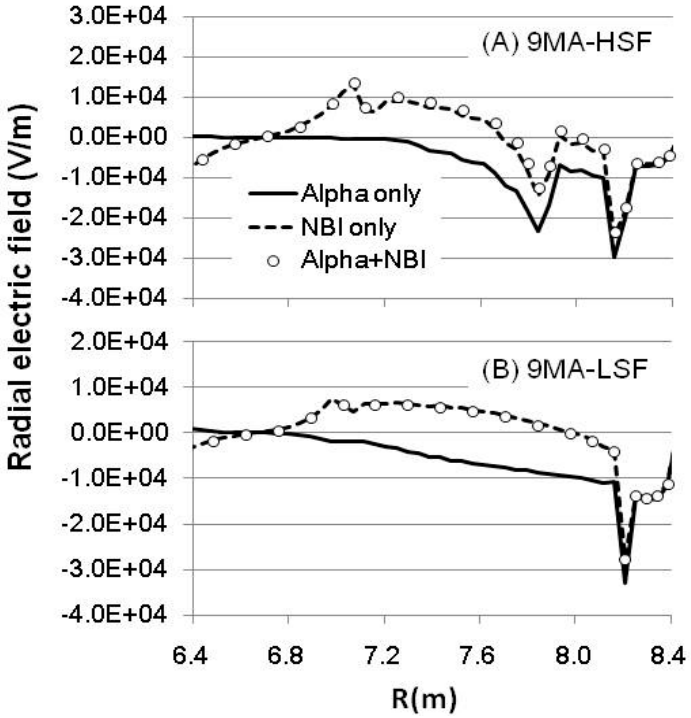

Figure 14. Radial distribution of the radial electric field for alpha-particle and NBI combined heating along the major radius on the midplane from the plasma center to the edge in the operation scenarios (A) 9MA-HSF and (B) 9MA-LSF.

The distribution of the radial electric field for alpha-particle and NBI combined heating along the major radius on the midplane from the plasma center to the edge are

shown in figure 14 for the operation scenarios 9MA-HSF and 9MA-LSF in (A) and (B), respectively. The radial distribution of the electric field for the combined heating is shown by the open circles. For reference, the distribution of the electric field for the separate alpha-particle and NBI heating shown in figure 12 is also plotted with solid and dashed curves, respectively. As shown in figure 8, the torque from NBI fast ions is much larger than that from alpha-particles in all the operation scenarios. Consequently, the electric field in the combined heating approximately coincides with that of separate NBI heating. Note that the magnitude of the negative electric field driven by separate alpha-heating is substantially reduced for combined heating. These findings indicate that the EF-enlargement factors of alpha particles losses for separate heating are substantially reduced for combined heating and those of NBI fast ions are approximately unchanged, which are consistent with the results shown in table 3.

Table 3 Summary of power losses of fast ions in TBM configuration for 9MA ITER operation scenarios with and without the electric field produced in NBI-Alpha combined heating.

Operation scenario	Non-axisymmetric field	Fast ions	Power Loss w/o EF (%)	Power Loss w/ EF (%)	Enlargement factor
9MA-HSF (Higer safety	TBM	Alpha	0.13	0.14	1.09
		NBI	0.017	0.050	2.94
9MA-LSF (Lower safety	TBM	Alpha	0.48	0.48	1.00
		NBI	0.015	0.084	5.60

5.1.2 Case TFR

We investigated the case of a magnetic field with non-axisymmetric components caused by a finite number of TF coils without ferritic insertions (TF-ripple) only for separate NBI and alpha-particle heating. The distribution of the magnetic field along the toroidal angle is shown in figure 2(B). The distribution of the field ripple on the plasma surface along the poloidal angle is shown in figure 3 by the dashed curve. The enlargement factors of the electric field on the power loss for alpha particles and NBI fast ions also are summarized in table 2. As shown in table 2, the effect of the electric field on the loss of fast ions in TF–ripples is very small in any operation scenario.

5.2 Results for the local transport of fast ions

In order to understand the global effects of the radial electric field on the confinement of fast ions, we looked into the local transport of fast ions only in the case of the 9MA-HSF scenario as an example. A diffusion coefficient of alpha particles was

estimated as a time-derivative of the variance of canonical angular momentum P_ϕ as follows;

$$D = \frac{1}{2}\frac{d}{dt}\left\langle \left(P_\phi - \left\langle P_\phi \right\rangle\right)^2 \right\rangle \Big/ \left(e_f \frac{d\psi}{dr}\right)^2 \quad , \tag{22}$$

where $\langle\ \rangle$ denotes the ensemble average over test particles.

As shown in figure 5, in a negative electric field, counter particles are more important since their banana tip moves outward, i.e., into a higher error field region. The transport of fast ions in a non-axisymmetric field is important for those particles near the plasma edge. For the numerical estimation of the diffusion coefficient, however, we chose points which were far enough away from the edge to prevent the effect of particle loss from having an impact upon the calculation of equation (22) using the OFMC code. Consequently, alpha particles were launched at $R = 7.9m$ on the mid plane with a velocity pitch $v_{//}/v = -0.259$. In order to highlight the effect of the electric field, a parabolic distribution of the electric potential which gives a radial electric field $E_r = -25.3kV/m$ at $R = 7.9m$ was adopted.

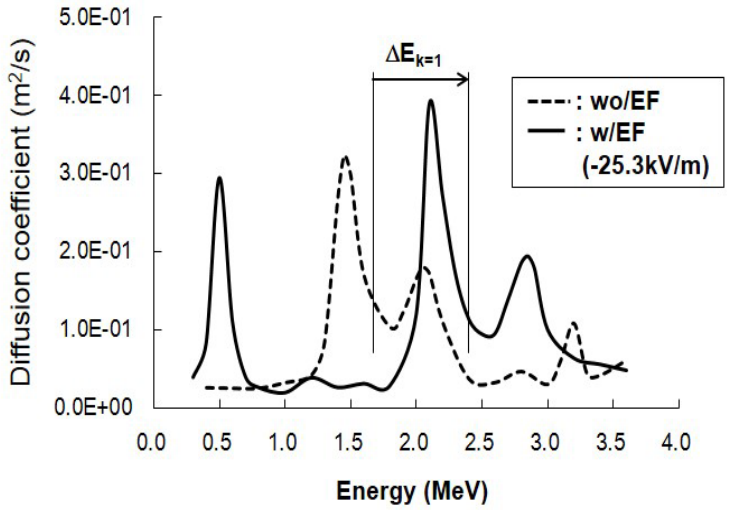

Figure 15. Energy dependence of the diffusion coefficient of alpha particles launched at $R = 7.9m$ on the mid-plane with a velocity pitch $v_{//}/v = -0.259$ (counter) in the error field caused by the TBMs in ITER. The radial electric field at $R = 7.9m$ is $E_r = -25.3kV/m$. The thick and thin curves show the diffusion coefficients with and without the electric field.

The diffusion coefficients of counter alpha particles are shown in figure 15 as

functions of the initial energy in the error field caused by the TBMs. The solid and the dashed curves show the diffusion coefficients with and without the EF. Generally, magnetic islands appear in an error magnetic field. Those particles which differ somewhat from the exact resonance condition and move around the separatrix of the islands undergo large radial displacement with small pitch angle scatterings. Consequently, the resonance diffusion coefficient has two peaks on both sides of the resonance energy which looks like the capital letter M [28]. The M-shaped resonance diffusions appear in the higher energy region in both cases with and without the EF. Note that the resonance energies move into a higher energy region in a negative radial electric field. The resonance energy change shown in figure 15 comes from the change in the toroidal precession caused by the EF.

Generally, the resonance condition of fast ions in a cyclic toroidal error field with a toroidal mode number n is given by

$$\varphi_{tpc} = \varphi_{tpc}^{\nabla B} + \varphi_{tpc}^{EF} = \frac{2k\pi}{n}, \quad k = 0, \pm 1, \pm 2, \pm 3, \text{L} . \tag{23}$$

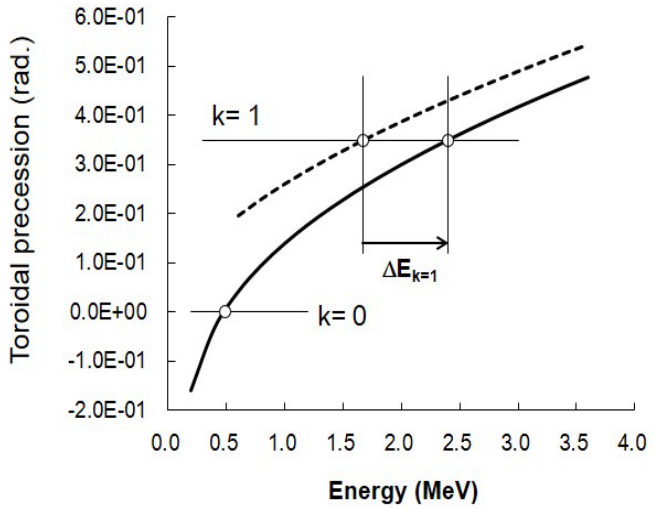

Figure 16. Energy dependence of the toroidal precession using the same calculation conditions as in figure 15. The solid and dashed curves show the toroidal precessions with and without the electric field

Figure 16 shows the energy dependence of the toroidal precession for *n=18* using the same calculation conditions as in figure 15. The solid and dashed curves show the toroidal precessions with and without the electric field. The resonance energies for $k = 1$ with and without the electric field shown in figure 16 approximately agree with those near the bottom of the M-shapes in figure 15 and the resonance peaks of the

diffusion coefficient appear on both sides of each resonance energy as described in reference [28]. This implies that even in a non-cyclic error field caused by TBMs in ITER (figure 2(A)), the resonance conditions approximately agree with those in a cyclic error field with a toroidal mode number n, if the toroidal angle difference between two adjacent TBMs is given by $2\pi/n$. Note that a large peak in the diffusion coefficient appears near $E \approx 0.5MeV$ which corresponds to the resonance for $k = 0$ in the electric field. Because the energy gap between the two peaks of the M-shaped resonance diffusion is proportional to the resonance energy [28], the energy gap for a low resonance energy when $k = 0$ becomes so small that the two peaks approximately overlap. Particles with $k = 0$ are toroidally locked without toroidal precession. Fast ions with a low toroidal precession due to the ∇B-drift can be toroidally locked by a negative radial electric field.

The positive shift in the resonance energy of a negative radial electric field indicates an increase in the power loss of fast ions during slowing down, because fast ions tend to escape from the plasma when they reach the resonance energy during slowing down. The effect of the radial electric field on the resonance energy, however, can be averaged to some extent among many particles. For example, those particles resonating in an electrically free field can be off resonance in an electric field and vice versa.

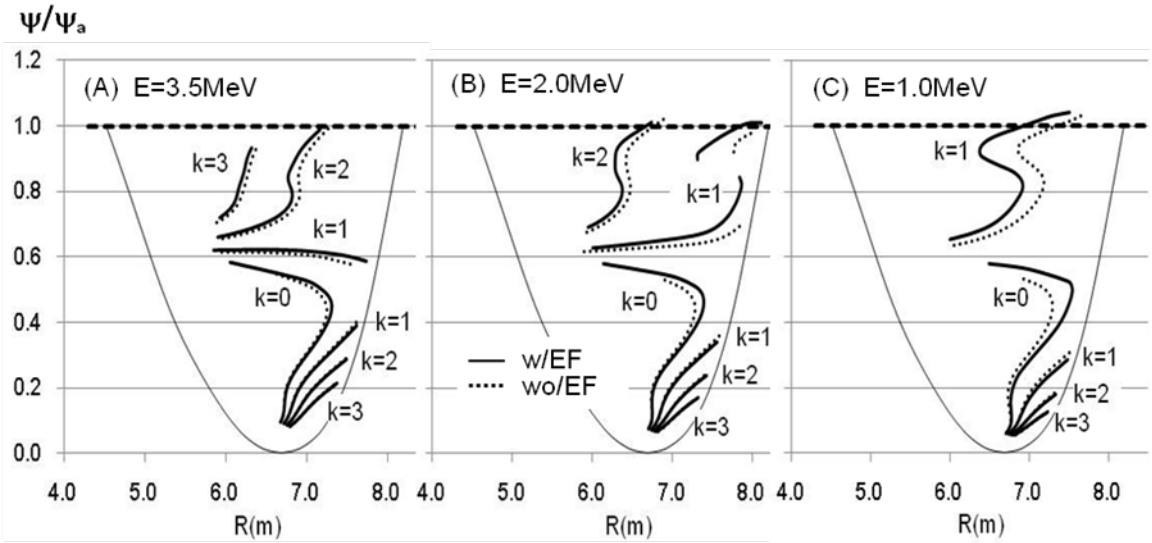

Figure 17. Resonance surfaces of alpha particles in the operation scenario 9MA-HSF for initial particle energies *E=3.5, 2.0* and *1.0 MeV* are shown in (A), (B) and (C), respectively. The thick solid curves show the resonance surfaces for the resonance parameter k=1,2 and 3 with the radial electric field given by the electric potential shown in figure 9(A-1) and the dotted curves without the field. The thin solid curves show the normalized poloidal flux function ψ/ψ_a along the midplane and the thick dashed lines at $\psi/\psi_a = 1.0$ indicate the plasma surface.

There are virtual surfaces formed by the banana-tip points of particles which satisfy the resonance conditions of equation (23) [29]. As such, we must consider another important effect of the radial EF on fast ion trajectory. The radial EF effectively changes the locations of the resonance surfaces. Figure 17 shows 2D cross-sectional views of the resonance surfaces of alpha particles with respect to the major radius and the normalized canonical angular momentum of tip points of resonating banana particles in the operation scenario 9MA-HSF for the resonance parameters *k=0,1,2* and *3*. The thin solid curves show the normalized poloidal flux function ψ/ψ_a along the midplane and the thick dashed lines at $\psi/\psi_a = 1.0$ indicate the plasma surface. The resonance surfaces with the electric field given by the electric potential shown in figure 9(A-1) are shown by the thick solid curves and those without the field by the dotted curves. Since the resonance condition depends on the particle energy, the resonance surfaces of alpha particles for the initial particle energies *E=3.5, 2.0* and *1.0MeV* are shown in figure 17(A), (B) and (C), respectively. Note that the resonance surfaces shift substantially due to the radial EF toward the plasma surface in the outer region and that the change in the radial position of the resonance surfaces is more significant for particles with lower energy.

Table 2 indicates that the EF effect on the loss of fast ions is very significant for those cases where the confinement of fast ions without the EF is basically good and vice versa. For example, the power-loss enlargement factors are relatively large in the cases of 9MA-HSF/TBM, 9MA-LSF/TBM and 15MA/TBM/NBI where fast ions are basically confined without the EF, whereas they are close to unity in all cases of TF ripple where the power losses without the EF are relatively large. The electric field near the plasma surface is very significant in the loss of fast ions. As shown in figure 12, the peaks of the electric field are localized near the plasma surface in all cases. In a large error field, particles near the plasma surface are lost even without the EF effect

As reviewed in section 4, there are three basic EF effects on the fast-ion trajectory; the effects on the banana tip point ΔR_{tip}^{EF} (equation (11)); on the banana width $\Delta\rho_B^{EF}$ (equation (17)); and on the toroidal precession φ_{tpc}^{EF} (corresponding to equation (20) in a circular plasma). In the presence of TBMs near the outer edge of the torus, the error field is localized near the mid-plane (θ=0) as shown in figure 3. If the electric field is negative, the banana-tip points of counter particles move into the higher ripple region. Consequently, the loss of fast ions tends to increase in a negative electric field and decrease in a positive electric field. The EF effect on the banana-tip point, however, is

very small as shown in figure 5. The contribution of the effect on the confinement of fast ions should be carefully investigated.

The EF effect on the toroidal precession can be evaluated by looking at the effective radial change of the resonance surfaces which is roughly given by Δr_{tpc}^{EF} (equation (21)). In order to figure out which effects are important for the confinement of fast ions in ITER, we evaluated both ratios of ΔR_{tip}^{EF} and $\Delta \rho_B^{EF}$ to $\left|\Delta r_{tpc}^{EF}\right|$ in the operation scenario 9MA-HSF for alpha particles with $E = 3.5MeV$ and $v_{//}/v = -0.174$ (counter). The ratios $\Delta R_{tip}^{EF} \Big/ \left|\Delta r_{tpc}^{EF}\right|$ and $\Delta \rho_B^{EF} \Big/ \left|\Delta r_{tpc}^{EF}\right|$ are shown in figure 18 by the dotted and the dashed curves, respectively. For reference, $\Delta r_{tpc}^{EF} \Big/ E_r$ is also shown by the solid curves.

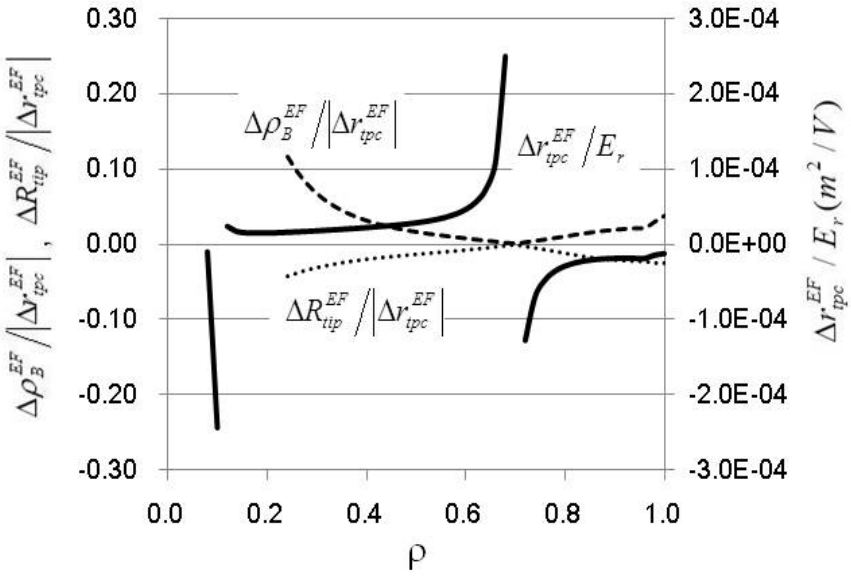

Figure 18. Radial distribution of $\Delta R_{tip}^{EF} \Big/ \left|\Delta r_{tpc}^{EF}\right|$ and $\Delta \rho_B^{EF} \Big/ \left|\Delta r_{tpc}^{EF}\right|$ in the operation scenario 9MA-HSF for alpha particles with $E = 3.5MeV$ and $v_{//}/v = -0.174$ (counter) are shown by the dotted and dashed curves, respectively. $\Delta r_{tpc}^{EF} \Big/ E_r$ also is shown by the solid curves

Note that the absolute values of both $\Delta R_{tip}^{EF} \Big/ \left|\Delta r_{tpc}^{EF}\right|$ and $\Delta \rho_B^{EF} \Big/ \left|\Delta r_{tpc}^{EF}\right|$ are much less than unity in most regions, especially in the region near the plasma edge ($\rho > 0.8$) where fast ion trajectories play an important role in their losses. This implies that the EF effect on the toroidal precession might be the main reason for the increase in fast ion

losses by the electric field in ITER with TBMs. It is also noted that $\Delta r_{tpc}^{EF} / E_r$ is singular and changes its sign at the point near $\rho \approx 0.7$ where $dq_s / dr = 0$. As shown in figure 12(A), the radial electric field driven by alpha particles is negative in the plasma region. The distribution of $\Delta r_{tpc}^{EF} / E_r$ shown in figure 18 and the negative electric field indicates that the radial movement of the resonance surfaces is outward (+) in the outer region and inward (-) in the inner region, which is consistent with the results shown in figure 17. In the region closer to the plasma center, $\Delta r_{tpc}^{EF} / E_r$ has another singular point at $\rho \approx 0.1$ and consequently the EF effect on the toroidal precession is significant in the operation scenario 9MA-HSF. The EF effect on the banana width near the plasma center might also be significant. The degradation of the power deposition profile of alpha particles near the plasma center shown in figure 13 (A) might be attributed to these EF effects, though it is difficult to evaluate their relative contributions, because $\Delta \rho_B^{EF}$ given by equation (17) diverges at the plasma center,

6. Summary

Conclusions of the present work can be summarized as follows:

1) The effects of the radial electric field (EF effect) on the losses of alpha particles and NBI fast ions in typical ITER operation scenarios for both error fields due to TBMs and TF ripple were evaluated using a method to execute an orbit-following Monte-Carlo code OFMC together with a one-dimensional transport code TASK/TX alternately and iteratively.
2) The EF effect on the loss of fast ions strongly depends on the operation scenario as well as on the error field. The electric field is very significant in the loss of fast ions for the 9MA-HSF operation scenario with an error field due to TBMs.
3) The EF effect in the error field of TF–ripple is very small in any operation scenario
4) The electric field is much more significant for the loss of NBI fast ions than for that of alpha particles in both separate and combined heating.
5) The radial electric field changes the toroidal precession of fast ions and consequently changes their resonance condition with the error field, which may be the main reason for the EF effect on the loss of fast ions in ITER with TBMs.

The EF effect on the confinement of fast ions in an error field is very sensitive to the distribution of the electric potential. We applied a one-dimensional transport code to evaluate the electric potential in the present work. For a more precise analysis, a non-circular transport code including the effect of momentum pinch should be applied in the future. Studies on the transport of fast ions near the plasma center also need to be made assiduously in the future.

One of the key issues concerning the loss of fast ions in a non-axisymmetric field lies in the resulting peak heat load on the first wall [29]. The power losses of fast ions which increase due to the radial EF in ITER are still acceptably small. Judging from the resonance surfaces modified by the radial EF shown in figure 17, the radial EF may cause a small change in the poloidal peak position of the heat load. In order to investigate such a small change in the peak heat load, an extremely large number of test particles is necessary. We leave this investigation for future work. Calculations using the most recent non-axisymmetric values for the magnetic field of ITER also will be made in the future.

Acknowledgment

The authors express their special thanks to Dr. M. Murakami for useful information on the electric field and plasma rotations in ITER using TRANSP. The authors are also

grateful to Prof. K. Itoh for useful discussion on the present issue. The authors appreciate the technical support provided by Dr. S. Ide and Mr. M. Suzuki, of JAEA for using the OFMC code. Dr. E. Tada is gratefully acknowledged for his continuous encouragement. The views and opinions expressed herein do not necessarily reflect those of the ITER Organization

References

[1] Krasheninnikov S.I. and Yushmanov P.N., 1994 Phys. Plasmas **1** 1186.

[2] Chankin A.V. and McCracken G.M. 1993 Nucl.Fusion **33** 1459.

[3] Miyamoto K. 1996 Nucl.Fusion **36** 927.

[4] Itoh K., Sanuki H., Itoh S|-I and Tani K. 1991 Nucl.Fusion **31** 1405.

[5] Polevoi A.R., et al., J. Plasma Fusion Res. SERIES, Vol. 5 (2002) 82-87.

[6] Tani K., Kishimoto H., et al. 1981 J. Phys. Soc. Japan **50** 1726.

[7] Honda M and Fukuyama A, 2008 J. Comput. Phys. **227** 2808.

[8] Honda M., Fukuyama A and Nakajima N. 2011 Journal of the Physical Society of Japan **80** 114502

[9] Honda M., Takizuka T., Tobita K., et al. 2011 Nucl. Fusion **51** 073018.

[10] Honda M., Fukuyama A and Nakajima N. 2011 Plasma and Fusion Resaerch **6** 1403008.

[11] Fukuyama A., Itoh K., Itoh S-I. et al. 1995 Plasma Phys. Control. Fusion **37** 611.

[12] Honda M., Fukuyama A., Takizuka T. and Shimizu K., 2010 Nucl. Fusion **50** 095012.

[13] Honda M., Ide S., Takizuka T. et al., 2013 Nucl. Fusion **53** 073050.

[14] Trubnikov B.A. 1965 Rev. Plasma Phys. **1** 105.

[15] 15MA: Polevoi A.R., et al., Proc. 37th EPS (2010, Dublin), P2.187.
9MA-LSF :Polevoi A.R., et al., Proc. 37th EPS (2010, Dublin), P2.187. ITER 15MA scenario calculated by ASTRA, 2009.

[16] Gribov Y., ITER document "Magnetic field produced by Test Blanket Modules", 2009.

[17] Tani K. and Azumi M. 2008 Nucl. Fusion **48** 085001

[18] Oikawa T., et al., Proc. PLASMA2014 (2014, Niigata)

[19] Oikawa T., et al., Proc. 24th Fusion Energy Conf. (2012, San Diego), ITR/P1-35.

[20] Ohnishi M., Tokunaga H. and Wakabayashi J., 1976 Nucl. Fusion **16** 690.

[21] Tani K., Takizuka T., Azumi M. and Kishimoto H., 1983 Nucl. Fusion 23 657.

[22] Goldston R.J. and Towner H.H., 1981 J. Plasma Phys. **26** 283,

[23] Goldston R.J., White R.B. and Boozer A.H., 1981 Rev. Lett. **47** 647.

[24] Davydenko V.I., Ivanov A.A., Karpushov A.N. et al. 1994 Plasma Phys. Controlled Fusion

36 1805.

[25] Hynönen V., Kurki-Suonio T., Suttrop W. et al. 2008 Plasma Phys. Control Fusion **50** 035014.

[26] Andreev V.V., Ilgisonis V.I. and Sorokina E.A. 2013 Phyics of Plasmas 20 122502.

[27] Yoshida M., Kaye S., Rice J. et al. 2012 Nucl. Fusion **52**

[28] Mimata H., Tani K., Tsutsui H. *et al* 2009 Plasma and Fusion Research **4** 008.

[29] Tani K., Shinohara K., Oikawa T et al. 2012 Nucl. Fusion **52** 013012.